

3D full-field biomechanical testing of a glenoid before and after implant placement

Yuxiao Zhou^a, Chujie Gong^b, Gregory S. Lewis^c, April D. Armstrong^c, Jing Du^{a,*}

^a Department of Mechanical Engineering, Pennsylvania State University, University Park, PA, United States of America

^b Department of Biomedical Engineering, Pennsylvania State University, University Park, PA, United States of America

^c Department of Orthopaedics and Rehabilitation, Penn State College of Medicine and M.S. Hershey Medical Center, Hershey, PA, United States of America

ARTICLE INFO

Article history:

Received 22 September 2019

Received in revised form 16 November 2019

Accepted 18 November 2019

Available online 21 November 2019

Keywords:

Glenoid

Strain

Micro-CT

ABSTRACT

Loosening of the glenoid component is the most common cause of failure of total shoulder arthroplasty. While the underlying mechanisms are not fully understood, mechanical factors are widely reported to play a key role in glenoid component loosening. In this study, mechanical testing coupled with micro X-ray computed tomography (micro-CT) is performed to apply various physiologically realistic loads on a native and implanted glenoid. Digital volume correlation of micro-CT images is used to compute the 3D full-field deformation and strain inside the glenoid. The measured strain distributions are in good agreement with the analytical solutions of beam bending models, especially for anteriorly and posteriorly eccentric loadings. The effective moduli of the overall native and implanted glenoid were similar. However, under the same eccentric loading conditions, implanted glenoid exhibited a wider range of strain, because the placement of glenoid component increases the bending moment inside the glenoid. This proof-of-concept study provides a feasible and powerful method for the study of 3D full-field biomechanics in native and implanted glenoids.

© 2019 Elsevier Ltd. All rights reserved.

1. Introduction

Total shoulder arthroplasty (TSA) is a common orthopaedic procedure to treat glenohumeral osteoarthritis [1,2]. Loosening of the glenoid component is the most common cause of failure of this procedure [3,4]. While the mechanisms underpinning glenoid loosening are not fully understood, mechanical factors are widely reported to play a key role [5–8]. There is a need to study the biomechanics of glenoid bone and the glenoid components in shoulder implants.

Numerical methods, such as finite element analysis, have often been used to compute the biomechanics of glenoid bone and glenoid implants [8,9]. The validity of the results from these models has been questioned, because these models may oversimplify the complex geometry, material properties and interface interactions in these structures. The results from these numerical models need to be validated by experimental measurements.

However, the conventional experimental methods for mechanical strain measurement in the research of biomechanics

for glenoid and glenoid components have various disadvantages. Most importantly, they are inherently limited to measuring external surface strains, instead of full-field internal strains. Conventional strain gauges [10–14] can only measure strain at single locations and need to be glued to a surface on the specimens. The photoelasticity method [15–17] needs to be performed on replica models made with photoelastic materials or on photoelastic sheets that are glued to bone specimens. To obtain Moiré fringe pattern [18,19], a grid of lines needs to be overlaid on the specimens.

Mechanical testing coupled with micro X-ray computed tomography (micro-CT) and digital volume correlation is a non-contact method that can measure the internal structures and mechanics concurrently. It has been used to measure strain in engineering materials [18,19], trabecular bone blocks [20–23] and glenoid specimens with the absence of implants [24]. In our prior work, we have extended this method to study the biomechanics of dental implants in mandibles and to build corresponding numerical models of the micro-structures [25,26].

In this study, mechanical testing coupled with micro-CT is carried out to apply various physiologically realistic loading conditions on a native and implanted glenoid. Digital volume correlation is performed to calculate the 3D full-field deformation and strain inside the glenoid. Analytical models, which incorporate the morphology measurements from the experiments, are developed to predict strain within the glenoid.

* Correspondence to: Penn State University, 316B Leonhard Building, University Park, PA16802, United States of America.

E-mail addresses: yyz5239@psu.edu (Y. Zhou), cwg5361@psu.edu (C. Gong), glewis1@pennstatehealth.psu.edu (G.S. Lewis), aarmstrong@pennstatehealth.psu.edu (A.D. Armstrong), jingdu@psu.edu (J. Du).

2. Materials and method

2.1. Mechanical testing coupled with micro-CT imaging

A fresh-frozen scapulae of upper extremity was obtained. The glenoid was isolated with the osteotomy being 44-mm medial to the glenoid face. All soft tissues were stripped off. The bottom half of the specimen was embedded in polymethylmethacrylate (PMMA, Ortho-Jet BCA, Lang Dental, Wheeling, IL) with the glenoid face surface parallel to the floor. The specimen was kept frozen at -23°C until 12-h prior to the test, when it was thawed. After completing the mechanical testing on native glenoid specimen, a commercially available glenoid implant (Bigliani/Flatow, Zimmer Inc., Warsaw, IN) was implanted into the glenoid specimen by a fellowship-trained, experienced shoulder surgeon using standard surgical technique. The glenoid component was positioned parallel with the glenoid face with no correction of alignment. The cementing technique for the glenoid required that cement (Palacos LV, Zimmer Inc., Warsaw, IN) be packed into the drilled peg holes on 2 occasions with a gauze sponge and then cement placed for a third time filling the holes before the implant was impacted into the bone. This allows for interdigitation of the cement into the glenoid trabecular bone [27]. The three-pegged polyethylene glenoid component had a diameter of 46 mm and a central metal pin that was removed to reduce image artifacts.

Mechanical testing was performed on the native glenoid and on the implanted glenoid, respectively, using a loading device (CT5000, Deben, Suffolk, UK) coupled with micro-CT (Phoenix v|tome|x L300 multi-scale micro-CT system, GE, Boston, MA). The loading setup was designed based on ASTM Standard F2028-17 [28], which was also adopted in other studies of implanted glenoids [29–32]. A compressive load was applied medially through a hemispherical polyoxymethylene humeral implant to mimic the contact loading in shoulder joints. The testing setup was adjusted to have glenohumeral contact point at three locations: (1) anteriorly eccentric; (2) at the center of the glenoid face (concentric); and (3) posteriorly eccentric, respectively.

The specimen was compressed at a rate of 0.1 mm/min until the load reached 750 N, with the displacement and load values recorded through the loading device. The load was held constant for ~ 1 h for the specimen to fully relax. Micro-CT scans were performed before loading and after the holding period. A voltage of 150 kV and a current of 160 μA was used in the scans. Image stacks with size of $2014 \times 2014 \times 2024$ voxels and isometric resolution of 35 μm were obtained.

2.2. Image processing and digital volume correlation (DVC)

The micro-CT images were downsized to 8-bit format in ImageJ (National Institute of Health, Maryland, USA) and were cropped to the region of interest in Avizo 3D analysis software (FEI Visualization Sciences Group, Burlington, MA). They were then segmented using the water-shed technique in Avizo. The humeral and glenoid implants, potting material and background were removed in the images. The regions of glenoid bone and bone cement were extracted for the following analysis. The image stacks at no-load and loaded conditions were registered in Avizo to make the medial part (bottom) of bone aligned with each other.

Digital volume correlation (DVC) was performed in DaVis software (LaVision, Goettingen, Germany) on the extracted images. The movements of each block of voxels were tracked by correlating the images at no-load and loaded states. A sequential correlation method was used, with the block size of 8.96, 4.48, and 2.24 mm, respectively in 3 correlation steps. The overlap ratio between adjacent blocks was chosen to be 50%. The deformation of the native and implanted glenoid specimen under

the above-mentioned 3 contact loading conditions was calculated, respectively. The strain was calculated as the gradient of deformation.

The noise level in the results was evaluated using a zero-strain approach [21–23,33]. Two sets of micro-CT scans were taken under no-load conditions. Theoretically, digital volume correlation of these two image sets results in zero deformation and zero strain. Hence, the non-zero computed deformation and strain characterized the uncertainties in the results.

2.3. Analytical models

An analytical model was developed to describe the strain on a virtual sagittal plane section in the glenoid under glenohumeral contact loading (Fig. 1). The virtual section was defined as an ellipse with the length of major axis $2a$ and the length of minor axis $2b$. Assuming the virtual section is far enough away from the glenoid face that the effects of Hertzian contact are negligible and assuming the homogeneity of the materials properties, the normal stress due to axial compression can be approximated by

$$\sigma_c = -\frac{F}{A} = -\frac{F}{\pi ab}$$

where F is the medio-lateral compressive load of 750 N, and A is the area of the elliptical section.

The bending moment on the virtual section could be attributed to the eccentric glenohumeral contact loading and the horizontal force component, which was also caused by the eccentricity of loading. It can be calculated by

$$M = F\delta + Ftan\theta \cdot \Delta$$

where δ is the distance between the glenohumeral contact point and the central axis of the glenoid, Δ is the distance between the glenohumeral contact point and the virtual section, and θ is the angle between the normal of glenohumeral contact surface and the central axis. Consequently, the maximum and minimum normal stress due to bending is given by

$$\sigma_b = \pm \frac{Mb}{I} = \pm \frac{(F\delta + Ftan\theta \cdot \Delta)b}{\frac{1}{4}\pi ab^3}$$

where I is the moment of inertia for the elliptical virtual section.

Assume small deformation and linear elasticity, the normal stress on the virtual section can be estimated by the superposition of axial compression and bending, and the normal strain on the virtual section can therefore be given by

$$\varepsilon = \frac{\sigma_c + \sigma_b}{E} = \frac{F}{E} \left[\frac{-1}{\pi ab} \pm \frac{4(\delta + \Delta tan\theta)}{\pi ab^2} \right]$$

where the effective modulus E is defined as the overall elastic modulus for the whole structure, including cortical and trabecular bone, implant and cement.

3. Results

3.1. Load-displacement relationships and stiffness

The load-displacement relationships obtained from the mechanical testing of native and implanted glenoid were nonlinear (Supplemental Fig. S1). The slopes of the load-displacement curves, i.e. stiffness of the specimen, increased with increasing displacement until the load reached 750 N. Then the load was held constant and the displacement kept increasing, reflecting the viscoelastic creep behaviors. For each loading condition, the native specimen was generally stiffer than the implanted specimen (Supplemental Fig. S1).

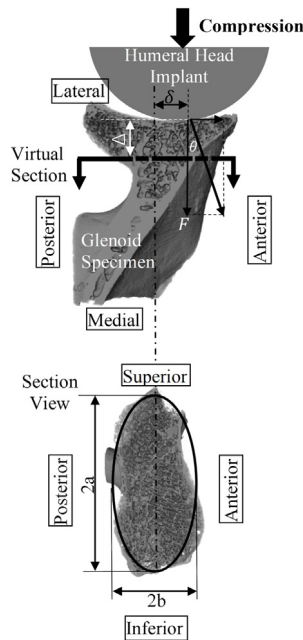


Fig. 1. Schematics of the analytical models geometry for the glenoid. The models describe the forces and strain on a virtual sagittal section in the glenoid under concentric and eccentric glenohumeral contact loading.

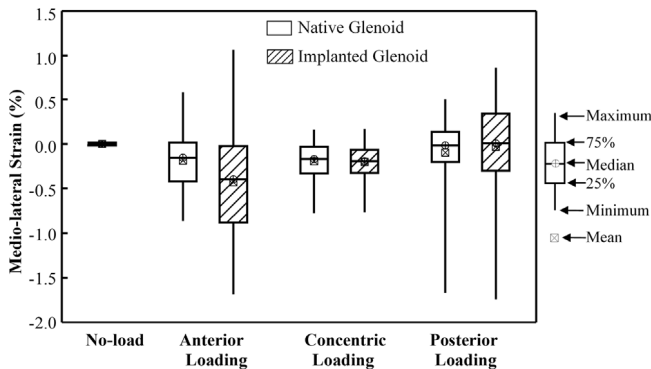


Fig. 2. Experimentally determined medio-lateral strain inside the native glenoid specimen and the implanted glenoid specimen under no-load, anterior, concentric, and posterior loading conditions. Positive strain indicates tension, whereas negative values indicates compression.

3.2. Deformation inside the glenoid

The magnitude of 3D deformation obtained from DVC (as described in Section 2.2) for each voxel block inside the specimen is presented in boxplot in Supplemental Fig. S2. Inside each specimen, there were about 45 000 voxel blocks with equal spacing of 1.12 mm in 3 coordinate directions between the centers of the blocks. The implanted glenoid exhibited a wider range of deformation than the native glenoid, under all 3 loading conditions. The two eccentric loading conditions resulted in wider ranges of deformation than those from concentric loading mode. In particular, the anteriorly eccentric loading led to wider range of deformation, compared with the posteriorly eccentric loading. The maximum deformation obtained from DVC of two image sets both taken at no-load conditions was around 0.022 mm, which is much smaller than average deformation under all 3 loading conditions.

Since the loading is along medio-lateral direction, the medio-lateral deformation contours before and after implantation and

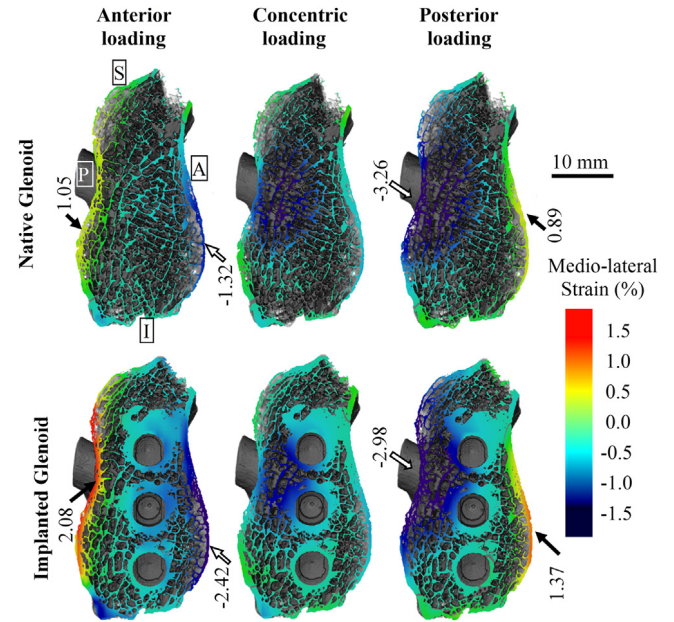


Fig. 3. Experimentally determined medio-lateral strain on a virtual sagittal section (5.7 mm below glenoid face) of the glenoid specimen before and after implant placement under anterior, concentric and posterior loading conditions. A – anterior, P – posterior, S – superior, and I – inferior.

under different loading conditions are discussed on a typical sagittal section with the distance to glenoid face of 5.7 mm. When the glenohumeral contact point was at the anterior side, the anterior part of the virtual section moved medially and the posterior part moved laterally. In contrast, for posterior glenohumeral contact loading, the virtual section exhibited lateral deformation on anterior side and medial deformation on posterior side. Under concentric loading condition, the deformation is more uniformly towards medial direction throughout the virtual section (Supplemental Fig. S3).

Before and after implantation, the trends of deformation distribution on the sagittal section are similar (Fig. S3). But the magnitudes of medio-lateral deformation were higher after the implant was placed. For example, under anterior loading, the maximum medial deformation was 0.26 mm and 0.58 mm at the anterior side of the section, in the native and implanted glenoid, respectively (Fig. S3). And, the maximum lateral deformation was 0.18 mm and 0.35 mm at the posterior side of the virtual section, in the native and implanted glenoid, respectively (Fig. S3).

In Fig. S3, it can also be noted on the sagittal section that the medio-lateral deformation on the anterior side had a higher magnitude than that on the posterior side, for any of the three loading conditions and for both the native glenoid and implanted glenoid. For example, when the implanted specimen was loaded posteriorly, the maximum lateral deformation at the anterior side (1.38 mm) was greater than the maximum medial deformation at the posterior side (0.77 mm).

3.3. 3D strain distribution inside glenoid specimens

The medio-lateral strain for each voxel block inside the glenoid was obtained from DVC (Section 2.2) and presented in the boxplot in Fig. 2. The top and bottom 3% of all data points were excluded. Although only compressive loadings were applied, both tensile and compressive strains existed inside the glenoid, ranging from -1.7% to 1.1% . The average strain values were compressive for anterior and concentric loading conditions, and near zero for

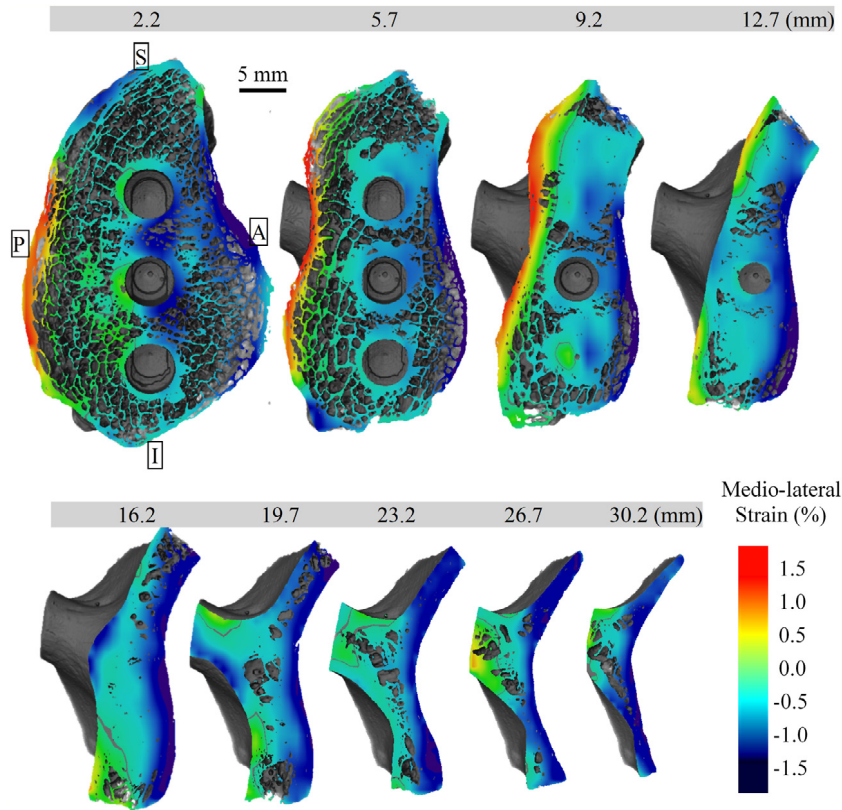


Fig. 4. Experimentally determined medio-lateral deformation under anterior loading on several virtual sagittal sections of the implanted glenoid specimen with the distances to the glenoid face varied. A – anterior, P – posterior, S – superior, and I – inferior.

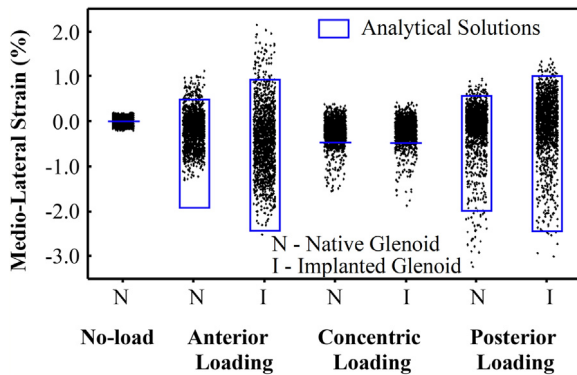


Fig. 5. Medio-lateral strain on a virtual sagittal section (5.7 mm below glenoid face) of the glenoid specimen before and after implant placement under anterior, concentric and posterior loading conditions. Scattered dots – measured from mechanical testing coupled with micro-CT; blocks – computed using analytical models.

posterior loading. The resulted strain ranges were wider under the two eccentric loading conditions than those under concentric loading. Under concentric loading, the native and implanted glenoid exhibited similar ranges of strain. However, under eccentric loadings, especially anterior loading, the strain in the implanted glenoid covered a wider range than that in the native glenoid. Under no-load condition, the medio-lateral strain ranged from -0.04% to 0.04% , which was much smaller than those under the loading conditions.

The medio-lateral strain contours on the same typical virtual section with the distance to glenoid face of 5.7 mm is presented in Fig. 3, for native and implanted glenoid and under different loading conditions. When the glenohumeral contact point was at

the anterior side, the strain was in compression in the anterior part of the virtual section and in tension in the posterior part. In contrast, for posterior glenohumeral contact loading, the strain was in tension in the anterior regions and in compression in the posterior regions. Under concentric loading, the strain is mostly in compression at the center of the virtual section and slightly in tension towards the edges (Fig. 3).

In native and implanted glenoid, the trends of strain distribution are similar. But the magnitudes of maximum and minimum strain were higher after the implant was placed (Fig. 3). Under anterior loading, the medio-lateral strain ranged from -0.86% to 0.58% in native glenoid and from -1.69% to 1.06% in implanted glenoid. Under posterior loading, the medio-lateral strain ranged from -1.68% to 0.50% in native glenoid and -1.75% to 0.86% in implanted glenoid.

There are some similarities in the trends of medio-lateral strain distribution on several virtual sections with different distances to the glenoid face (Fig. 4). With the glenoid component implanted and under anterior loading, the anterior sides of these sections were usually under compression whereas the posterior side sometimes under tension. The magnitudes of compressive strain were similar on these sections, but the magnitude of tensile strain increased as the distance to the glenoid face reduced.

3.4. Analytical solutions

The analytical model was applied to calculate the strain distribution on the same typical virtual section with the distance to glenoid face of 5.7 mm. The geometry factors (Eccentric loading distance δ , distance of virtual section Δ , and contact loading angle θ) were measured using the micro-CT images for the various conditions (Table 1). The lengths of the semi-major and semi-minor axes of the virtual section were measured to be 19 mm and

Table 1

The geometry factors of the native and implanted glenoid specimen under different loading conditions. These parameters were measured from micro-CT images of the specimen and were used in the analytical models.

Loading condition	Native glenoid			Implanted glenoid		
	Anterior	Concentric	Posterior	Anterior	Concentric	Posterior
Eccentric loading distance δ (mm)	2.4	0	1.7	2.68	0	1.97
Distance of virtual section Δ (mm)	6.43	6.00	6.88	10.15	9.60	10.17
Contact loading angle θ	10.23°	0	17.26°	11.58°	0	16.22°

8.5 mm, respectively. The effective modulus of the native and implanted glenoid specimen was chosen as 208 MPa and 202 MPa, respectively, such that more than 90% of the strain values measured from the experiments fall in the range of strain predicted by the analytical model, for native and implanted glenoid under anterior and posterior loading conditions. The ranges of strain calculated using the analytical model are in good agreement with experimental measurements (Fig. 5). Under concentric loading, the model can only predict the lower bound of strain, whereas the strain measured from experiments was not uniform (Figs. 3 and 5).

4. Discussion

The results of this study show that the mechanical testing coupled with micro-CT is a feasible and powerful method to characterize 3D full-field deformation and strain inside native and implanted glenoids. The noise in the results (no-load in Fig. 2 and Fig. S2) was much smaller than the range of deformation or strain inside glenoid under glenohumeral joint contact loading. The measured strain distributions on a typical virtual section of the specimen were in good agreement with the results predicted by the analytical model (Fig. 5).

When interpreting the results, it is important to note that the measured deformation was the overall deformation for each block of voxels that were used in the digital volume correlation processes. Each voxel block may contain trabecular bone, cortical bone and/or bone cement. Hence the measured strain was the nominal strain for the voxel blocks. In regions of porous trabecular bone, this strain reflected nominal strain but not the tissue strain in individual trabeculae. In regions that included a combination of materials, the strain reflected the overall average strain. Similarly, in the analytical model, the effective modulus was defined as the overall elastic modulus for the whole structures, including cortical and trabecular bone, implant and cement.

The effective moduli of the native and implanted glenoid predicted by the analytical model both fell in the range of nominal elastic moduli of glenoid trabecular bone measured experimentally in several prior works [34–36]. Also, in the analytical models, the difference between the effective moduli for the native and implanted glenoid was less than 3%. However, the strain inside the implanted glenoid spanned a much wider range than that inside the native glenoid (Fig. 2). The increased strain range can mostly be attributed to the thickness of glenoid component, which increased the distance between the glenohumeral contact point and the virtual section plane (Table 1), thus increased the bending moment on the virtual section.

The discrepancies in the strain values under concentric loading condition obtained from experiments and the analytical models (Fig. 5) can be greatly attributed to the ball-and-socket geometry of glenohumeral joint. In the experiments, under concentric loading, the strain was not uniformly distributed on the virtual section, but concentrated at the center of the virtual section (Fig. 3), especially on those sections that were close to the glenoid face (Fig. 4). Conversely, the analytical models assumed equal strains across the entire section; the model can be improved by incorporating Hertzian contact into the loading modes.

The physiological loading conditions are more complicated than the simplified mechanical loadings that were applied in the experiments in this study. In physiological conditions, the glenohumeral contact loading can be more complicated than the experimental setup in this study, including greater eccentric distance and different abduction angles [5,37,38]. Nevertheless, the experiments in this study were designed based on the ASTM standard for assessing glenoid loosening [28], and the loads applied in the experiments fall in the range of physiologically realistic loading conditions.

Another limitation of the current study is that of only one glenoid specimen was studied, although both native and implanted conditions were tested under anteriorly eccentric, concentric and posteriorly eccentric conditions. Thus, a systematic study with larger sample size and rigorous statistical analysis is recommended as an area for future work to generalize the results to the population.

5. Conclusions

This paper presents the results of 3D full-field biomechanical testing of a glenoid before and after implant placement. The deformation and strain inside a native and implanted glenoid under several physiologically realistic loading conditions were obtained by digital volume correlation of micro-CT images taken at no-load and loaded conditions. Under glenohumeral contact loading, especially eccentric contact loading, part of the specimen was under compression while part was under tension. The measured strain distributions were in good agreement with the analytical solutions of beam bending models, especially for anteriorly and posteriorly eccentric loadings. The effective moduli of the overall native and implanted glenoid were similar. However, under the same eccentric loading conditions, implanted glenoid exhibited wider range of strain, because the insertion of glenoid implant component increased the distance from the glenohumeral contact point to the same locations in the glenoid, therefore increased the bending moment in the glenoid. Despite some drawbacks of the method, this proof-of-concept study provided a feasible and strong method to map the 3D full-field deformation and strain in native and implanted glenoids.

Declaration of competing interest

Dr. A. Armstrong is a paid consultant for Zimmer Biomet and Globus, and we acknowledge that all other authors do not have any conflict of interest. Authors were fully involved in the study and preparation of the manuscript.

Acknowledgments

The authors are grateful to Dr. Timothy Ryan and Mr. Timothy Stecko at the Center for Quantitative Imaging (CQI) at Penn State University, United States of America for technical support on micro-CT scans. Appreciation is also extended to Mr. Richard Prevost at LaVision for useful technical discussions.

Appendix A. Supplementary data

Supplementary material related to this article can be found online at <https://doi.org/10.1016/j.eml.2019.100614>.

References

- [1] K. Issa, et al., Total shoulder arthroplasty demographics, incidence, and complications—a nationwide inpatient sample database study, *Surg. Technol. Int.* (2016).
- [2] J.E. Hsu, D.J. Hackett, K.V. Vo, F.A. Matsen, What can be learned from an analysis of 215 glenoid component failures? *J. Shoulder Elb. Surg.* (2018).
- [3] T.J. Fox, A. Cil, J.W. Sperling, J. Sanchez-Sotelo, C.D. Schleck, R.H. Cofield, Survival of the glenoid component in shoulder arthroplasty, *J. Shoulder Elb. Surg.* 18 (6) (2009) 859–863.
- [4] K.I. Bohsali, M.A. Wirth, C.A. Rockwood, Complications of total shoulder arthroplasty, *J. Bone Joint Surg. Am.* 88 (10) (2006) 2279–2292.
- [5] D.F. Massimini, G. Li, J.P. Warner, Glenohumeral contact kinematics in patients after total shoulder arthroplasty, *J. Bone Joint Surg. Am.* 92 (4) (2010) 916–926.
- [6] T. Gregory, et al., Glenoid loosening after total shoulder arthroplasty: An in vitro CT-scan study, *J. Orthop. Res.* 27 (12) (2009) 1589–1595.
- [7] P. Westerhoff, et al., In vivo measurement of shoulder joint loads during activities of daily living, *J. Biomech.* 42 (12) (2009) 1840–1849.
- [8] Y. Chevalier, I. Santos, P.E. Müller, M.F. Pietschmann, Bone density and anisotropy affect periprosthetic cement and bone stresses after anatomical glenoid replacement: A micro finite element analysis, *J. Biomech.* (2016).
- [9] W. Pomwenger, K. Entacher, H. Resch, P. Schuller-Götzburg, Need for CT-based bone density modelling in finite element analysis of a shoulder arthroplasty revealed through a novel method for result analysis, *Biomed. Tech. (Berl.)* 59 (5) (2014) 421–430.
- [10] S.C. Mordecai, S.M. Lambert, J.M. Meswania, G.W. Blunn, I.L. Bayley, S.J.G. Taylor, An experimental glenoid rim strain analysis for an improved reverse anatomy shoulder implant fixation, *J. Orthop. Res.* 30 (6) (2012) 998–1003.
- [11] L. Pauzenberger, et al., Biomechanical evaluation of glenoid reconstruction with an implant-free j-bone graft for anterior glenoid bone loss, *Am. J. Sports Med.* 45 (12) (2017) 2849–2857.
- [12] J.D. Borstad, A. Dashottar, Quantifying strain on posterior shoulder tissues during 5 simulated clinical tests : A cadaver study, *J. Orthop. Sport. Phys. Ther.* 41 (2) (2011) 90–99.
- [13] A.R. Karduna, G.R. Williams, J.P. Iannotti, J.L. Williams, Total shoulder arthroplasty biomechanics: A study of the forces and strains at the glenoid component, *J. Biomech. Eng.* 120 (1) (1998) 92.
- [14] G.C. Terry, D. Hammon, P. France, L.A. Norwood, The stabilizing function of passive shoulder restraints, *Am. J. Sports Med.* 19 (1) (1991) 26–34.
- [15] L.A. Murphy, P.J. Prendergast, Acromion-fixation of glenoid components in total shoulder arthroplasty, *J. Biomech.* 38 (8) (2005) 1702–1711.
- [16] M.H. Pelletier, A. Langdown, R.M. Gillies, D.H. Sonabend, W.R. Walsh, Photoelastic comparison of strains in the underlying glenoid with metal-backed and all-polyethylene implants, *J. Shoulder Elb. Surg.* 17 (5) (2008) 779–783.
- [17] R.D. Peindl, M.E. Harrow, P.M. Connor, D.M. Banks, D.F. D'Alessandro, Photoelastic stress freezing analysis of total shoulder replacement systems, *Exp. Mech.* 44 (3) (2004) 228–234.
- [18] B. Croom, W.-M. Wang, J. Li, X. Li, Unveiling 3D deformations in polymer composites by coupled micro X-ray computed tomography and volumetric digital image correlation, *Exp. Mech.* 56 (6) (2016) 999–1016.
- [19] B.P. Croom, et al., Damage mechanisms in elastomeric foam composites: Multiscale X-ray computed tomography and finite element analyses, *Compos. Sci. Technol.* 169 (2018) 195–202.
- [20] O. Jiroušek, I. Jandajsek, D. Vavřík, Evaluation of strain field in microstructures using micro-CT and digital volume correlation, *J. Instrum.* 6 (01) (2011) C01039.
- [21] B.K. Bay, T.S. Smith, D.P. Fyhrie, M. Saad, Digital volume correlation : Three-dimensional strain mapping using x-ray tomography, *Exp. Mech.* 39 (3) (1999) 217–226.
- [22] E. Verhulp, B. Van Rietbergen, R. Huisjes, A three-dimensional digital image correlation technique for strain measurements in microstructures, *Exp. Mech.* 37 (2004) 1313–1320.
- [23] R. Zauel, Y.N. Yeni, B.K. Bay, X.N. Dong, D.P. Fyhrie, Comparison of the linear finite element prediction of deformation and strain of human cancellous bone to 3D digital volume correlation measurements., *J. Biomech. Eng.* 128 (1) (2006) 1–6.
- [24] J. Kusins, N. Knowles, M. Ryan, E. Dall'Ara, L. Ferreira, Performance of QCT-Derived scapula finite element models in predicting local displacements using digital volume correlation, *J. Mech. Behav. Biomed. Mater.* 97 (2019) 339–345.
- [25] J. Du, et al., Biomechanics and strain mapping in bone as related to immediately-loaded dental implants., *J. Biomech.* 48 (12) (2015) 3486–3494.
- [26] Q. Mao, K. Su, Y. Zhou, M. Hossaini-Zadeh, G.S. Lewis, J. Du, Voxel-based micro-finite element analysis of dental implants in a human cadaveric mandible: Tissue modulus assignment and sensitivity analyses, *J. Mech. Behav. Biomed. Mater.* 94 (2019) 229–237.
- [27] W.W. Flint, G.S. Lewis, H.B. Wee, B.J. Bryce, A.D. Armstrong, Glenoid cement mantle characterization using micro-computed tomography of three cement application techniques, *J. Shoulder Elb. Surg.* 25 (4) (2016) 572–580.
- [28] American Society for Testing and Materials, in: *Standard Test Methods for Dynamic Evaluation of Glenoid Loosening or Disassociation*, ASTM International, 2014.
- [29] M.D. Budge, M.D. Kurdziel, K.C. Baker, J.M. Wiater, A biomechanical analysis of initial fixation options for porous-tantalum-backed glenoid components, *J. Shoulder Elb. Surg.* 22 (5) (2013) 709–715.
- [30] J.P. Iannotti, K.E. Lippin, C.L. Klotz, E.W. Reber, S.W. Swope, Lift-off resistance of augmented glenoid components during cyclic fatigue loading in the posterior-superior direction, *J. Shoulder Elb. Surg.* 22 (11) (2013) 1530–1536.
- [31] V.J. Sabesan, J. Ackerman, V. Sharma, K.C. Baker, M.D. Kurdziel, J.M. Wiater, Glenohumeral mismatch affects micromotion of cemented glenoid components in total shoulder arthroplasty, *J. Shoulder Elb. Surg.* 24 (5) (2018) 814–822.
- [32] T. Wang, G.D. Abrams, A.W. Behn, D. Lindsey, N. Giori, E.V. Cheung, Posterior glenoid wear in total shoulder arthroplasty: Eccentric anterior reaming is superior to posterior augment, *Clin. Orthop. Relat. Res.* 473 (12) (2015) 3928–3936.
- [33] M.R. Hardisty, C.M. Whyne, Whole bone strain quantification by image registration: A validation study, *J. Biomech. Eng.* 131 (6) (2009) 064502.
- [34] H.H. Bayraktar, E.F. Morgan, G.L. Niebur, G.E. Morris, E.K. Wong, T.M. Keaveny, Comparison of the elastic and yield properties of human femoral trabecular and cortical bone tissue, *J. Biomech.* 37 (1) (2004) 27–35.
- [35] C. Anglin, P. Tolhurst, U.P. Wyss, D.R. Pichora, Glenoid cancellous bone strength and modulus, *J. Biomech.* 32 (10) (1999) 1091–1097.
- [36] L.H. Frich, N.C. Jensen, A. Odgaard, C.M. Pedersen, J.O. Sjøbjerg, M. Dalstra, Bone strength and material properties of the glenoid., *J. Shoulder Elb. Surg.* 6 (2) (1997) 97–104.
- [37] R.E. Debski, E.K. Wong, S.L.Y. Woo, M. Sakane, F.H. Fu, J.P. Warner, In situ force distribution in the glenohumeral joint capsule during anterior-posterior loading, *J. Orthop. Res.* 17 (5) (1999) 769–776.
- [38] N. Andarawis-Puri, A.F. Kuntz, M.L. Ramsey, L.J. Soslowsky, Effect of glenohumeral abduction angle on the mechanical interaction between the supraspinatus and infraspinatus tendons for the intact, partial-thickness torn, and repaired supraspinatus tendon conditions, *J. Orthop. Res.* 28 (7) (2010) 846–851.